

An anode-free Li metal cell with replenishable Li designed for long cycle life



Haodong Liu^a, John Holoubek^a, Hongyao Zhou^a, Zhaohui Wu^a, Xing Xing^a, Sicen Yu^a, Gabriel M. Veith^b, Yeqing Li^a, Meng Hu^a, Yoonjung Choi^a, Ping Liu^{a,*}

^a Department of NanoEngineering, University of California San Diego, 9500 Gilman Drive, La Jolla, CA, 92093, USA

^b Materials Science and Technology Division, Oak Ridge National Laboratory, Oak Ridge, TN, 37831, USA

ARTICLE INFO

Keywords:
Anode-free Li metal cell
Li metal anode
Suppress “dead” Li
Replenishable Li
Long cycle life

ABSTRACT

Pit corrosion of Li during stripping is an important factor responsible for poor Li cycling efficiency, a metric that determines its cycling life. When excess Li is present, it has been observed that Li tends to strip in a non-uniform fashion, forming pits that extend well past the theoretical Li depth that inevitably lead to the formation of electronically isolated “dead” Li particles. In this work, a novel cell with replenishable Li is shown to inherently mitigate the formation of this “dead” Li, as a direct result of a design in which the intrinsically more homogenous stripping behavior of anode-free cells are combined with a replenishable limited Li reservoir. These novel cells ($\text{Li}|\text{Cu}||\text{LiFePO}_4$) exhibit 25% and 34% higher cumulative capacities than the conventional cells ($\text{Cu}|\text{Li}||\text{LiFePO}_4$) in carbonate and ether electrolytes, respectively, enabling a significant increase in cycle life without impacting energy density. This improvement strategy represents a new direction in Li metal battery improvement, in which improved cycling can be achieved regardless of electrolyte chemistry.

1. Introduction

The pathway towards 500 Wh kg⁻¹ rechargeable batteries has been proposed recently by the Battery 500 Consortium, where the key to achieving such a metric is the employment of Li metal as the anode [1–4]. However, the volume expansion and inherent reactivity of Li generally results in low coulombic efficiency and dendritic growth that yields a short cycle life and potential safety risks for any practical Li metal battery [5–9]. In the past decade, several important strategies have been widely studied for improving the cycle life of the Li metal anode, including designing novel electrolytes, [10–18] protecting the surface of the Li, [19–25] constructing 3D porous hosts, [26–31] and engineering the cell design [32,33].

To date, realizing high coulombic efficiency Li metal anodes is still the biggest challenge, where the accumulation of the electrochemically inactive “dead” Li has been identified as a primary limitation [34,35]. Besides the electronically disconnected, SEI (solid electrolyte interface) surrounded “dead” Li that is formed during plating, “dead” Li particles are also inevitably formed during stripping due to non-homogenous flux over repeated cycles [36,37]. Indeed, pit formation marches through the entire Li electrode thickness even when only a fraction of the Li was supposed to be cycled.

Li-free batteries, on the other hand, provide all the active Li for plating by the cathode. Due to the inevitable side reactions during the initial

charge in order to form the SEI, the cell capacities are always limited by the amount of active lithium. Couple with the poor coulombic efficiency during subsequent cycles, the cells usually experience rapid capacity decay. However, the Li-free batteries provide one advantage, in that all the active Li of the plated Li metal is stripped at the end of cell discharge, effectively mitigating the effect of pit formation. In this work, we describe a novel anode free cell design that maintains this advantage. However, an active Li reserve is also provided in order to extend the cell cycle life. This design significantly reduced buildup of “dead” Li, enhancing the cycle life of the constructed Li metal battery.

2. Experimental methods

2.1. Electrolyte preparation

The solvents ethylene carbonate (EC), ethylmethyl carbonate (EMC), 1,3-dioxolane (DOL), 1,2-dimethoxyethane (DME), vinylene carbonate (VC), and the salt lithium hexafluorophosphate (LiPF_6) were purchased from Gotion and used as received. Lithium bis(fluorosulfonyl)imide (LiFSI) and lithium nitrate (LiNO_3) were purchased from Sigma Aldrich. Lithium bis(trifluoromethane sulfonyl)imide (LiTFSI) was purchased from Capchem. The two electrolytes of 1.2 M LiPF₆ in EC/EMC (1:1 weight ratio) with 2wt% of VC, and 1 M LiFSI, 1 M LiTFSI, and 0.5 M LiNO₃ in DOL/DME (1:1 weight ratio) were prepared by dissolving

* Corresponding author.

predetermined amounts of salts into the mixed solvents under stirring to achieve stable and clear solutions. Here, 1 M is defined as 1 M salt dissolved into 1 kg of solvent.

2.2. Preparation of electrodes

LiFePO_4 (LFP) cathodes were prepared with LiFePO_4 powder (MTI corporation), Super-P, graphite, and PVDF in a ratio of 75:10:5:10 mixed in N-methyl pyrrolidinone (NMP) and cast on Al foil. After drying in a vacuum oven at 80°C overnight, the LiFePO_4 cathode was cut into 12 mm discs with an active areal mass loading of $\sim 18.2 \text{ mg cm}^{-2}$.

For stripping characterization, $40 \pm 5 \mu\text{m}$ thin commercial Li was obtained from China Energy Lithium Co.. The limited thin Li film used in cell testing was prepared via electrochemical plating in a $\text{Cu}||\text{Li}$ coin cell. The electrolyte for making the thin Li film was 1 M LiFSI, 1 M LiTFSI, and 0.5 M LiNO_3 in DOL/DME (1:1 weight ratio), which resulted in a dendrite free dense Li film, which was retrieved from the $\text{Li}||\text{Cu}$ cell and paired with an LFP electrode for full cell studies. A 12.5 mm-diameter Li chip was used to deposit 2 mAh cm^{-2} of Li on a 15 mm-diameter Cu foil at 0.1 mA cm^{-2} for the $\text{Cu}|\text{Li}||\text{LFP}$ cells. Another 6 mm-diameter Li chip was used to deposit 8 mAh cm^{-2} of Li on a 15 mm-diameter Cu foil under 0.1 mA cm^{-2} for the $\text{Li}|\text{Cu}||\text{LFP}$ cells. In all cases, the deposited Li films were washed with DME, then dried in the glovebox for 1 hour before use.

2.3. Electrochemical test

2016-type coin cells were used for all the electrochemical performance studies in this work with Celgard 25 μm trilayer PP-PE-PP membranes as the separator. One 1-mm thick spacer was placed on the anode side under the Li electrode to match the thickness of the cell stack to the coin cell case. A fixed amount of electrolyte ($\sim 50 \mu\text{L}$) was added into each coin cell to guarantee the complete wetting of the separator and electrodes.

In the $\text{Cu}|\text{Li}||\text{LFP}$ cell, the 2 mAh cm^{-2} Li (12.5 mm in diameter) was placed on the spacer, where the Li faced to the LFP cathode, as in a common Li battery cell. The size of the Li film was slightly larger than the LFP cathode to ensure good alignment of the electrodes. In the $\text{Li}|\text{Cu}||\text{LFP}$ cell, the 8 mAh cm^{-2} Li (6 mm in diameter) was placed on the spacer on top of which was placed a Cu foil (Li was thus on the side of Cu not facing the LFP cathode). A drop of electrolyte was added between the spacer and Li to guarantee the wetting of the Li during cycling. The small size of the Li film in this cell was designed for minimizing the Li participation in the normal cycling process due to the large distance between the edge of the Li and the LFP electrode. In both configurations, the total Li metal amount is the same.

Galvanostatic charge/discharge was conducted between a cell voltage of 2 to 4 V. The first charge/discharge cycle was conducted at 0.2 mA cm^{-2} , and the following cycles were under 0.5 mA cm^{-2} . Once the capacity of the $\text{Li}|\text{Cu}||\text{LFP}$ cell dropped below 75% of the original output capacity of the cell, Li was replenished to the cathode. After the normal discharge to 2 V at 0.5 mA cm^{-2} , the cell was rested for an hour to reach the equilibrium of the cell potential followed by discharging the cell to 2 V at 0.02 mA cm^{-2} . Afterwards, the cell was rested for another hour and was discharged to 2 V at 0.01 mA cm^{-2} again. In order to have a fair comparison, the same two-step discharge at low current densities was also applied to the $\text{Cu}|\text{Li}||\text{LFP}$ cell, when its capacity dropped below 75% of the original output.

Galvanostatic cycling was conducted on a Land battery tester. For *ex-situ* characterization, the cycled electrodes were recovered by disassembling the coin cell. All the samples were washed with pure electrolyte solvents three times and dried in the glovebox antechamber under vacuum.

The electrochemical impedance spectrum (EIS) was measured on cells at the fully discharged state at a frequency from 7 MHz to 0.1 Hz on an electrochemical working station (Biologic).

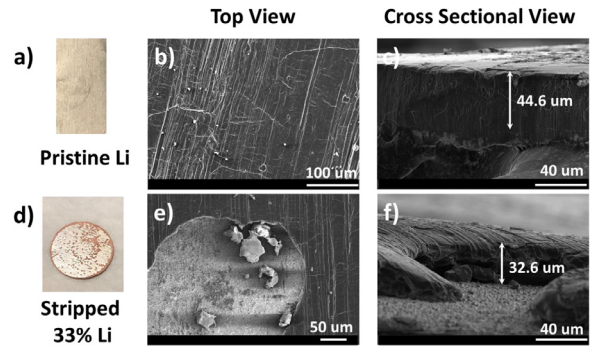


Fig. 1. a) Optical image of the $40 \pm 5 \mu\text{m}$ commercial thin Li. b) Top view SEM image of the $40 \pm 5 \mu\text{m}$ commercial thin Li. c) Cross-sectional SEM image of the $40 \pm 5 \mu\text{m}$ commercial thin Li. d) Optical image of the $40 \pm 5 \mu\text{m}$ commercial thin Li after stripping Li under 0.5 mA cm^{-2} for 6 h. e) Top view SEM image of the $40 \pm 5 \mu\text{m}$ commercial thin Li after stripping Li under 0.5 mA cm^{-2} for 6 h. f) Cross-sectional SEM image of the $40 \pm 5 \mu\text{m}$ commercial thin Li after stripping Li under 0.5 mA cm^{-2} for 6 h. Electrolyte is 1.2 M LiPF_6 in EC/EMC (1:1 weight ratio) with 2 wt% of VC.

2.4. Characterization

The morphology and thickness of the Li metal films were characterized using scanning electron microscopy (SEM, FEI Quanta 250 SEM). The sample was attached to a double-sided carbon tape and placed on a specimen holder. The prepared sample was sealed in a laminate plastic bag inside the glovebox for transferring to the SEM. The approximate time of sample exposed to air (from a sealed environment to the SEM stage) was less than 3 s.

3. Results and discussions

3.1. Direct observation of pit corrosion during Li Stripping

As a demonstration, pit corrosion based Li stripping dynamics were observed by directly stripping a commercial $40 \pm 5 \mu\text{m}$ thick Li foil at 0.5 mA cm^{-2} . The pristine Li foil presents a smooth surface, its thickness is measured as $44.6 \mu\text{m}$ (Fig. 1a-c). As shown in Fig. 1d, the Cu substrate was found to be exposed after only 3 mAh cm^{-2} ($\sim 33\%$) of the Li was electrochemically stripped. On this non-uniform Li substrate, $\sim 10 \mu\text{m}$ -sized isolated Li particles were observed via scanning electron microscopy (SEM) (Fig. 1e). Besides the isolated Li particles, the thickness of the partially stripped Li foil was non-uniform, which ranges from 0 to $32.6 \mu\text{m}$ (Fig. 1f).

3.2. The design of the novel anode free cell with replenishable Li

The impact of such “dead” Li formation on the operation of a conventional LMB is depicted in Fig. 2a, where the formation of isolated Li particles over repeated cycles eventually consumes all of the available excess Li, resulting in an exponential decay in capacity [34,35,37]. As a comparison, the anode free LMB in Fig. 2b only plates/strips Li from the cathode, where the reversible capacity of the cell degrades from the first cycle. While pit corrosion in anode free LMBs is significantly diminished from limited Li LMBs, their cycle life is typically too low to be employed. Our decoupled anode free cell with replenishable Li (Fig. 2c) seeks to mitigate this issue, where a replenishable Li reservoir is placed on the back of the Cu anode, which allows the battery to operate as an anode free cell during standard rate charging and discharging due to the greatly increased impedance of the diffusion path to the Li reservoir, all the while producing minimal “dead” Li from pit corrosion. After the output capacity of this decoupled anode free cell decreases below a set threshold, the capacity is replenished from the reservoir through an

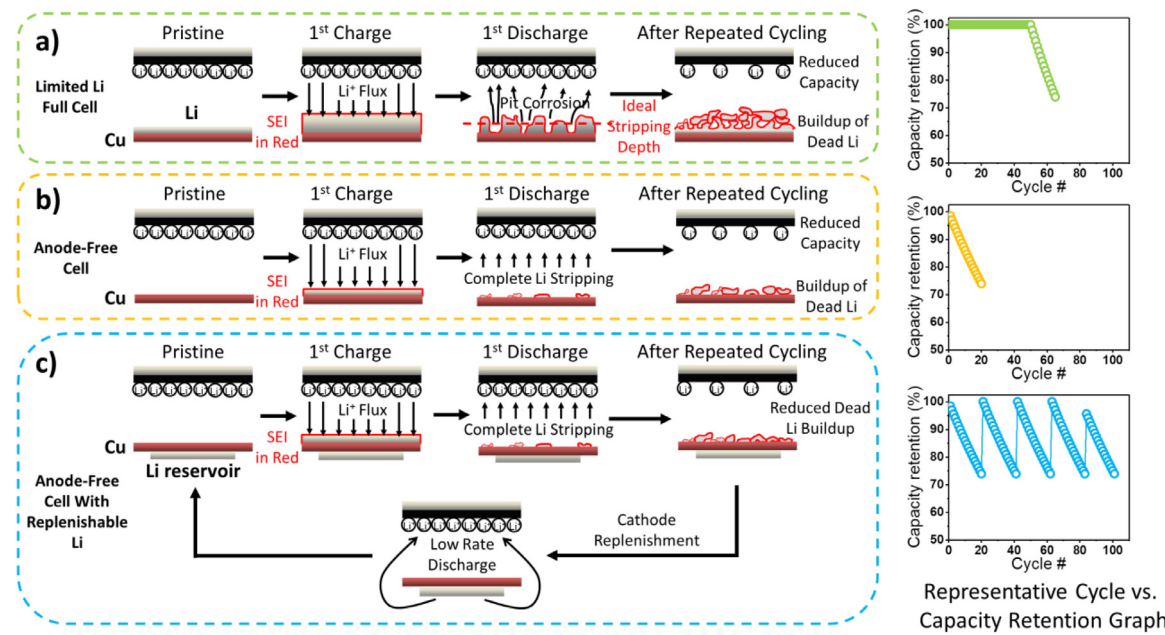


Fig. 2. The schematics of the three different cell configurations. a) Limited Li full cell. b) Anode-free full cell. c) Anode-free full cell with replenishable Li.

extremely low-rate lithiation. This cell design and operation scheme results in a cycle life longer than either limited Li and anode free cells while maintaining the energy density of the former.

3.3. The performance of $\text{Li}|\text{Cu}||\text{LiFePO}_4$ cell in carbonate electrolyte

To assemble these cells, 12.5 mm diameter Li films (2 mAh cm^{-2}) and 6 mm in diameter Li films with areal capacity of 8 mAh cm^{-2} were first prepared via electrochemical deposition on Cu substrates in ether electrolyte at 0.1 mA cm^{-2} (Fig. S1-2) to ensure the same starting morphology and excess Li capacity of 2.26 mAh . The electrochemically deposited Li films were found to consist of closely packed Li particles with diameters of $\sim 20 \mu\text{m}$. The thickness of the 2 mAh cm^{-2} Li and the 8 mAh cm^{-2} Li were $11.5 \mu\text{m}$ and $41.9 \mu\text{m}$, respectively, which are close to the theoretical thickness of 100% dense Li [29].

The performance of the cells was firstly evaluated in 1.2 M LiPF_6 in EC/EMC (1:1 wt) + 2 wt % VC electrolyte. The prepared anodes were paired with LFP cathodes at a N/P ratio of ~ 0.8 , in which the 12.5 mm and 6 mm Li films were assembled facing towards, and away from the LFP, respectively (Fig. S3). Henceforth, these cells will be referred to as $\text{Cu}|\text{Li}||\text{LFP}$, and $\text{Li}|\text{Cu}||\text{LFP}$, which were tested by continuous charge/discharge cycling at 0.5 mA cm^{-2} between 2 - 4 V until their capacity retention dropped below 75% (Fig. 3a & c and Fig. S4). We estimate that the Li^+ diffusion path between Li and LFP cathode in $\text{Cu}|\text{Li}||\text{LFP}$ is $25 \mu\text{m}$ (the thickness of the Celgard separator), and the path in $\text{Li}|\text{Cu}||\text{LFP}$ is at least 6 mm (> 240 times longer). Because of the greatly increased impedance due to the long diffusion path to the Li reservoir in $\text{Li}|\text{Cu}||\text{LFP}$, the battery operates as an anode free cell during standard rate charging and discharging with almost no access to the Li reservoir. After 10 cycles, the specific capacity of the LFP in $\text{Li}|\text{Cu}||\text{LFP}$ dropped to 96.8 mAh g^{-1} (Fig. 3d). The normal discharge current density at 0.5 mA cm^{-2} was not able to access the Li reservoir (Fig. S5). A low current density discharge at 0.02 mA cm^{-2} was performed to replenish the LFP capacity, which recovered the specific capacity of the LFP to 129 mAh g^{-1} . Afterwards, the $\text{Li}|\text{Cu}||\text{LFP}$ was further discharged at 0.01 mA cm^{-2} . The specific capacity of the LFP in $\text{Li}|\text{Cu}||\text{LFP}$ was replenished to a combined 131.4 mAh g^{-1} after the two slow discharge steps. As a comparison, the specific capacity of the LFP of the typical $\text{Cu}|\text{Li}||\text{LFP}$ decreased to 98.6 mAh g^{-1} after 26 cycles where all the excess Li was already consumed. To provide a fair comparison, the two slow dis-

charge steps were also applied to this cell, where the specific capacity of the LFP was found to slightly increase to 101.3 mAh g^{-1} (Fig. 3b). We note that the same two-step discharge at low current densities was applied to both the replenishment design and the conventional design. In the former, the two step discharge serves to replenish the capacity from the Li reservoir; in the later, the slow discharge helps to extract more capacity as well (some lithium in the conventional design can be accessed at low rates). As shown in Fig. 3a & c, the $\text{Cu}|\text{Li}||\text{LFP}$ delivered cumulative capacities (sum of output capacity over all cycles) of $60.53 \text{ mAh cm}^{-2}$, while the $\text{Li}|\text{Cu}||\text{LFP}$ exhibited higher cumulative capacities of $75.69 \text{ mAh cm}^{-2}$ (25 % improvement).

The morphologies of the cycled Li in the two cells were investigated by SEM (Fig. 4 and Fig. S6). Fig. 4a-d presents the morphology of the Li from the $\text{Cu}|\text{Li}||\text{LFP}$, where both dendritic Li and isolated “dead” Li particles were observed. The $\sim 5 \mu\text{m}$ “dead” Li particles were found to be randomly distributed in the cycled Li film, which is likely induced by the pit corrosion, consistent with the previous stripping experiments [36]. These metallic Li particles are not accessible even at slow discharge currents, and contribute to the short lifetime of the $\text{Cu}|\text{Li}||\text{LFP}$ cell. Additionally, there is an extreme increase in Li thickness from $11.5 \mu\text{m}$ to $93.1 \mu\text{m}$ over the cycle lifetime, corresponding to an extreme increase in porosity. Although the cycled Li from the $\text{Li}|\text{Cu}||\text{LFP}$ also exhibited dendritic Li, which is commonly observed in carbonate electrolytes, there was no observable “dead” Li, indicating the utilization of the Li in $\text{Li}|\text{Cu}||\text{LFP}$ is higher than the Li in $\text{Cu}|\text{Li}||\text{LFP}$. Furthermore, the thickness of the cycled Li in the $\text{Li}|\text{Cu}||\text{LFP}$ cell was found to be $39.3 \mu\text{m}$ after the complete depletion of the replenishable Li reservoir. The optical image and SEM image of the Li reservoir at the end of the cell life indicated the near full utilization of the Li reservoir (Fig. S7).

3.4. The performance of $\text{Li}|\text{Cu}||\text{LiFePO}_4$ cell in ether electrolyte

In order to confirm that the novel cell design also improves cycle lifetime utilizing electrolytes with higher intrinsic Li CE, a 1 M LiFSI , 1 M LiTFSI , and 0.5 M LiNO_3 in DOL/DME (1:1 wt) electrolyte was utilized for the same cycling test. It was found for this ether electrolyte, the typical $\text{Cu}|\text{Li}||\text{LFP}$ cell reached 75% capacity retention at the 90th cycle (Fig. 5a & Fig. S8), and the extra two slow discharge steps partially recovered the specific capacity of the LFP to 117.5 mAh g^{-1} (Fig. 5b), suggesting that the SEI layer on the isolated Li particles was not com-

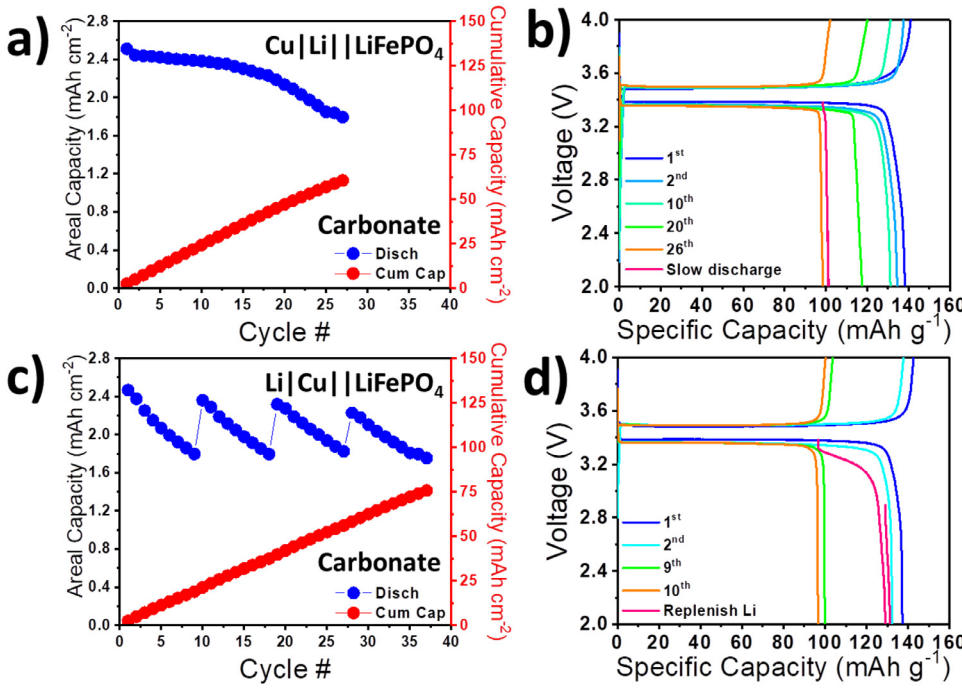


Fig. 3. The cycling performance of the limited Li full cells. a) $\text{Cu}|\text{Li}| \text{LiFePO}_4$ and c) $\text{Li}|\text{Cu}| \text{LiFePO}_4$ cells utilizing the 1.2 M LiPF_6 in EC/EMC (1:1 wt) + 2 wt % VC electrolyte. b) Voltage profiles of the $\text{Cu}|\text{Li}| \text{LiFePO}_4$ cell. d) Voltage profiles of the $\text{Li}|\text{Cu}| \text{LiFePO}_4$ cell. The first charge/discharge is under 0.2 mA cm^{-2} , the following cycles are under 0.5 mA cm^{-2} , once the capacity of the cell drops below 75% of the original capacity of the cell, Li is replenished to the cathode by firstly discharging at 0.02 mA cm^{-2} , then another discharge step at 0.01 mA cm^{-2} .

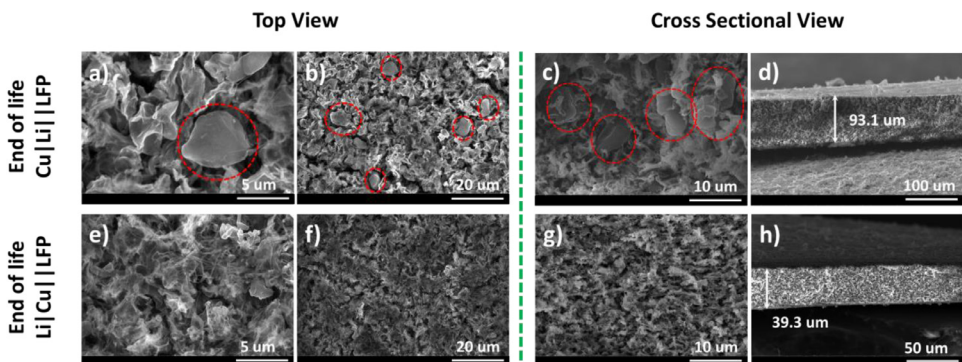


Fig. 4. SEM images of the Li anodes at the end of the cycle life of the cells. a) and b) Top view of the Li from the $\text{Cu}|\text{Li}| \text{LiFePO}_4$ cell. c) and d) Cross-sectional view of the Li from the $\text{Cu}|\text{Li}| \text{LiFePO}_4$ cell. e) and f) Top view of the Li from the $\text{Li}|\text{Cu}| \text{LiFePO}_4$ cell. g) and h) Cross-sectional view of the Li from the $\text{Li}|\text{Cu}| \text{LiFePO}_4$ cell.

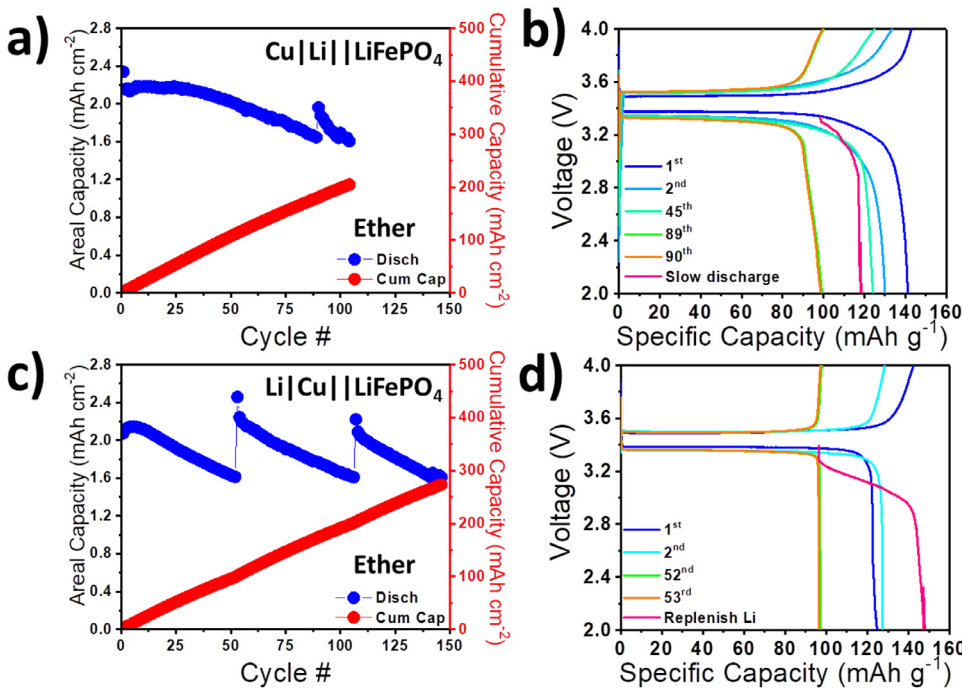


Fig. 5. The cycling performance of the limited Li full cells. a) $\text{Cu}|\text{Li}| \text{LiFePO}_4$ and c) $\text{Li}|\text{Cu}| \text{LiFePO}_4$ cells utilizing the 1 M LiTFSI , 1 M LiNO_3 , and 0.5 M LiTFSI in DOL/DME (1:1 weight ratio) electrolyte. b) Voltage profiles of the $\text{Cu}|\text{Li}| \text{LiFePO}_4$ cell. d) Voltage profiles of the $\text{Li}|\text{Cu}| \text{LiFePO}_4$ cell. The first charge/discharge is under 0.2 mA cm^{-2} , the following cycles are under 0.5 mA cm^{-2} , once the capacity of the cell drops below 75% of the original capacity of the cell, Li is replenished to the cathode by firstly discharging at 0.02 mA cm^{-2} , then another discharge step at 0.01 mA cm^{-2} .

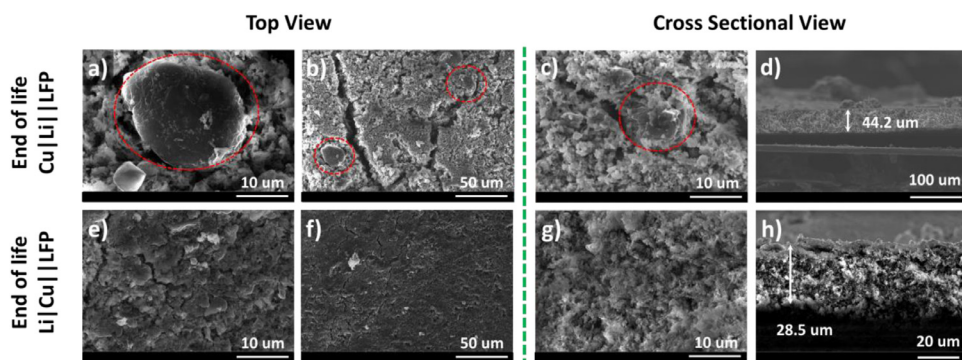


Fig. 6. SEM images of the Li anodes at the end of the cycle life of the cells. a) and b) Top view of the Li from the Cu|Li||LFePO₄ cell. c) and d) Cross-sectional view of the Li from the Cu|Li||LFePO₄ cell. e) and f) Top view of the Li from the Li|Cu||LFePO₄ cell. g) and h) Cross-sectional view of the Li from the Li|Cu||LFePO₄ cell.

pletely insulating and a certain amount of the isolated Li particles were still accessible. Overall, the Cu|Li||LFP cell reached 75% capacity retention at the 104th cycles (including slow discharge steps), corresponding to cumulative capacities of 204.65 mAh cm⁻². The improved cycle life of these cells compared to those utilizing carbonate electrolytes is likely a result of the higher CE of Li cycling in the ether system. In contrast, the decoupled Li|Cu||LFP cells did not fail until the 146th cycle, corresponding to a cumulative capacity of 273.42 mAh cm⁻² (34 % improvement) (Fig. 5c & d).

These cells were also disassembled to investigate the Li morphology of the Cu|Li||LFP cell, where SEM images still revealed large electronically isolated Li particles, and an increase in Li thickness from 11.5 μm to 44.2 μm (Fig. 6a-d) despite the relatively high intrinsic CE and dendrite-free morphology of the ether system. The decoupled Li|Cu||LFP cells showed improved Li deposition, where no isolated Li particles were observed, and the thickness of the cycled Li was found to be 28.5 μm after full utilization of the replenishable Li reservoir (Fig. 6e-h). These Li films were also characterized by X-ray Photoelectron Spectroscopy (XPS) to reveal the chemical species of their SEI layers. Both of the Li films showed C-SO_x, S=O, C-F, S-Ox, Li-S, and LiF signals on their surface (Fig. S9), [11,12] indicating their SEI are dominated by the reduction products of the LiTFSI and LiFSI salts. Since the Cu|Li||LFP and Li|Cu||LFP were cycled in the same electrolyte, the compositions of SEI on their Li were very similar. Additionally, the advantage of our novel cell design is more evident at high charge/discharge current density, where cycling tests at 2 mA cm⁻² yielded cumulative capacities of 132.64 mAh cm⁻² and 191.16 mAh cm⁻² for the Cu|Li||LFP and Li|Cu||LFP cells, respectively, which corresponds to a 44% enhancement (Fig. S10).

Electrochemical impedance spectroscopy (EIS) of the cells employing the ether electrolyte was also conducted at the end of their cycle lives (Fig. S11). The semicircles at high-frequency regions represent the interfacial resistance at the electrode/electrolyte interface [30,38]. The Cu|Li||LFP cell shows a high interfacial resistance of 1682 Ω, whereas the Li|Cu||LFP displayed a significantly reduced R_{SEI} of 59.94 Ω. The high interfacial resistance explains that the large electronically isolated Li particles in Cu|Li||LFP cell are not accessible even at an extremely low discharge current density. It also explains the higher voltage polarization in Cu|Li||LFP cell.

4. Conclusion

In summary, pit corrosion generated inactive Li was found to limit the cycle life of LMB full cells, and was significantly mitigated by a novel decoupled anode free cell with replenishable Li, resulting in significantly improved cycle lives at the same energy density. The decoupled Li|Cu||LFePO₄ cell produced a 34% and 44% cycling improvement at 0.5 mA cm⁻² and 2 mA cm⁻², respectively in an ether electrolyte. The new cell design is expected to be compatible with other advanced electrolyte systems, and promises inherently improved cycle lives for high energy density LMBs.

Supporting Information. The morphologies of the thin Li films used in this study. The comparison of Cu|Li||LFePO₄ and Li|Cu||LFePO₄ cells cycled in different electrolytes. SEM of cycled Li from Cu|Li||LFePO₄ and Li|Cu||LFePO₄ cells after 9 cycles. XPS of cycled Li from Cu|Li||LFePO₄ and Li|Cu||LFePO₄ cells. EIS of cycled Cu|Li||LFePO₄ and Li|Cu||LFePO₄ cells.

Declaration of Competing Interest

The authors declare that they have no known competing financial interests or personal relationships that could have appeared to influence the work reported in this paper.

CRediT authorship contribution statement

Haodong Liu: Conceptualization, Data curation, Formal analysis, Investigation, Methodology, Project administration, Supervision, Visualization, Writing - original draft, Writing - review & editing. **John Holoubek:** Formal analysis, Investigation, Validation, Visualization, Writing - review & editing. **Hongyao Zhou:** Formal analysis, Investigation, Methodology, Visualization. **Zhaohui Wu:** Investigation, Resources. **Xing Xing:** Formal analysis, Methodology. **Sicen Yu:** Investigation, Visualization. **Gabriel M. Veith:** Investigation, Methodology, Resources. **Yejing Li:** Visualization. **Meng Hu:** Investigation, Resources. **Yoonjung Choi:** Investigation, Resources, Validation. **Ping Liu:** Conceptualization, Funding acquisition, Project administration, Supervision, Writing - review & editing.

Acknowledgment

This work was supported by the Office of Vehicle Technologies of the U.S. Department of Energy through the Advanced Battery Materials Research (BMR) Program (Battery500 Consortium) under Contract No. DE-EE0007764. Part of the work used the UCSD-MTI Battery Fabrication Facility and the UCSD-Arbin Battery Testing Facility.

Supplementary materials

Supplementary material associated with this article can be found, in the online version, at doi:[10.1016/j.ensm.2020.12.032](https://doi.org/10.1016/j.ensm.2020.12.032).

References

- [1] J. Liu, Z. Bao, Y. Cui, E.J. Dufek, J.B. Goodenough, P. Khalifah, Q. Li, B.Y. Liaw, P. Liu, A. Manthiram, Y.S. Meng, V.R. Subramanian, M.F. Toney, V.V. Viswanathan, M.S. Whittingham, J. Xiao, W. Xu, J. Yang, X.-Q. Yang, J.-G. Zhang, Pathways for practical high-energy long-cycling lithium metal batteries, Nat. Energy (2019).
- [2] C.J. Niu, H. Lee, S.R. Chen, Q.Y. Li, J. Du, W. Xu, J.G. Zhang, M.S. Whittingham, J. Xiao, J. Liu, High-energy lithium metal pouch cells with limited anode swelling and long stable cycles, Nat. Energy 4 (7) (2019) 551–559.
- [3] D.-H. Liu, Z. Bai, M. Li, A. Yu, D. Luo, W. Liu, L. Yang, J. Lu, K. Amine, Z. Chen, Developing high safety Li-metal anodes for future high-energy Li-metal batteries: strategies and perspectives, Chem. Soc. Rev. 49 (15) (2020) 5407–5445.

- [4] X.B. Cheng, R. Zhang, C.Z. Zhao, Q. Zhang, Toward safe lithium metal anode in rechargeable batteries: a review, *Chem. Rev.* 117 (15) (2017) 10403–10473.
- [5] K.N. Wood, M. Noked, N.P. Dasgupta, Lithium metal anodes: toward an improved understanding of coupled morphological, electrochemical, and mechanical behavior, *ACS Energy Lett.* 2 (3) (2017) 664–672.
- [6] X.-B. Cheng, C. Yan, X.-Q. Zhang, H. Liu, Q. Zhang, Electronic and ionic channels in working interfaces of lithium metal anodes, *ACS Energy Lett.* 3 (7) (2018) 1564–1570.
- [7] X. He, Y. Yang, M.S. Cristian, J. Wang, X. Hou, B. Yan, J. Li, T. Zhang, E. Paillard, M. Swietoslawski, R. Kostecki, M. Winter, J. Li, Uniform lithium electrodeposition for stable lithium-metal batteries, *Nano Energy* 67 (2020) 104172.
- [8] F. Sun, D. Zhou, X. He, M. Osenberg, K. Dong, L. Chen, S. Mei, A. Hilger, H. Markötter, Y. Lu, S. Dong, S. Marathe, C. Rau, X. Hou, J. Li, M.C. Stan, M. Winter, R. Dominko, I. Manke, Morphological reversibility of modified Li-based anodes for next-generation batteries, *ACS Energy Lett.* 5 (1) (2020) 152–161.
- [9] F. Sun, X. He, X. Jiang, M. Osenberg, J. Li, D. Zhou, K. Dong, A. Hilger, X. Zhu, R. Gao, X. Liu, K. Huang, D. Ning, H. Markötter, L. Zhang, F. Wilde, Y. Cao, M. Winter, I. Manke, Advancing knowledge of electrochemically generated lithium microstructure and performance decay of lithium ion battery by synchrotron X-ray tomography, *Mater. Today* 27 (2019) 21–32.
- [10] L. Yu, S. Chen, H. Lee, L. Zhang, M.H. Engelhard, Q. Li, S. Jiao, J. Liu, W. Xu, J.-G. Zhang, A localized high-concentration electrolyte with optimized solvents and lithium difluoro(oxalate)borate additive for stable lithium metal batteries, *ACS Energy Lett.* 3 (9) (2018) 2059–2067.
- [11] X. Ren, L. Zou, S. Jiao, D. Mei, M.H. Engelhard, Q. Li, H. Lee, C. Niu, B.D. Adams, C. Wang, J. Liu, J.-G. Zhang, W. Xu, High-concentration ether electrolytes for stable high-voltage lithium metal batteries, *ACS Energy Lett.* 4 (4) (2019) 896–902.
- [12] X. Cao, X.D. Ren, L.F. Zou, M.H. Engelhard, W. Huang, H.S. Wang, B.E. Matthews, H. Lee, C.J. Niu, B.W. Arey, Y. Cui, C.M. Wang, J. Xiao, J. Liu, W. Xu, J.G. Zhang, Monolithic solid-electrolyte interphases formed in fluorinated orthoformate-based electrolytes minimize Li depletion and pulverization, *Nat. Energy* 4 (9) (2019) 796–805.
- [13] X. Xing, Y. Li, X. Wan, V. Petrova, H. Liu, P. Liu, Cathode electrolyte interface enabling stable Li-S batteries, *Energy Storage Mater.* (2019).
- [14] S.R. Chen, J.M. Zheng, D.H. Mei, K.S. Han, M.H. Engelhard, W.G. Zhao, W. Xu, J. Liu, J.G. Zhang, High-voltage lithium-metal batteries enabled by localized high-concentration electrolytes, *Adv. Mater.* (21) (2018) 30.
- [15] S.R. Chen, J.M. Zheng, L. Yu, X.D. Ren, M.H. Engelhard, C.J. Niu, H. Lee, W. Xu, J. Xiao, J. Liu, J.G. Zhang, High-efficiency lithium metal batteries with fire-retardant electrolytes, *Joule* 2 (8) (2018) 1548–1558.
- [16] L.M. Suo, W.J. Xue, M. Gobet, S.G. Greenbaum, C. Wang, Y.M. Chen, W.L. Yang, Y.X. Li, J. Li, Fluorine-donating electrolytes enable highly reversible 5-V-class Li metal batteries, *P Natl. Acad. Sci. USA* 115 (6) (2018) 1156–1161.
- [17] X. Fan, L. Chen, O. Borodin, X. Ji, J. Chen, S. Hou, T. Deng, J. Zheng, C. Yang, S.-C. Liou, K. Amine, K. Xu, C. Wang, Non-flammable electrolyte enables Li-metal batteries with aggressive cathode chemistries, *Nat. Nanotechnol.* 13 (8) (2018) 715–722.
- [18] H. Liu, J. Holoubek, H. Zhou, A. Chen, N. Chang, Z. Wu, S. Yu, Q. Yan, X. Xing, Y. Li, T.A. Pascal, P. Liu, Ultrahigh coulombic efficiency electrolyte enables Li||SPAN batteries with superior cycling performance, *Mater. Today* (2020).
- [19] X. Bi, K. Amine, J. Lu, The importance of anode protection towards lithium oxygen batteries, *J. Mater. Chem. A* 8 (7) (2020) 3563–3573.
- [20] H. Zhou, S. Yu, H. Liu, P. Liu, Protective coatings for lithium metal anodes: Recent progress and future perspectives, *J. Power Sources* 450 (2020) 227632.
- [21] H.D. Liu, X.F. Wang, H.Y. Zhou, H.D. Lim, X. Xing, Q.Z. Yan, Y.S. Meng, P. Liu, Structure and solution dynamics of lithium methyl carbonate as a protective layer for lithium metal, *ACS Appl. Energy Mater.* 1 (5) (2018) 1864–1869.
- [22] H. Liu, H. Zhou, B.-S. Lee, X. Xing, M. Gonzalez, P. Liu, Suppressing lithium dendrite growth with a single-component coating, *ACS Appl. Mater. Interfaces* 9 (36) (2017) 30635–30642.
- [23] Y. Gao, Z.F. Yan, J.L. Gray, X. He, D.W. Wang, T.H. Chen, Q.Q. Huang, Y.G.C. Li, H.Y. Wang, S.H. Kim, T.E. Mallouk, D.H. Wang, Polymer-inorganic solid-electrolyte interphase for stable lithium metal batteries under lean electrolyte conditions, *Nat. Mater.* 18 (4) (2019) 384–.
- [24] X.B. Cheng, R. Zhang, C.Z. Zhao, F. Wei, J.G. Zhang, Q. Zhang, A review of solid electrolyte interphases on lithium metal anode, *Adv. Sci.* (3) (2016) 3.
- [25] X.Q. Zhang, X.B. Cheng, Q. Zhang, Advances in interfaces between Li metal anode and electrolyte, *Adv. Mater. Interfaces* 5 (2) (2018).
- [26] H. Zhao, D. Lei, Y.-B. He, Y. Yuan, Q. Yun, B. Ni, W. Lv, B. Li, Q.-H. Yang, F. Kang, J. Liu, Compact 3D copper with uniform porous structure derived by electrochemical dealloying as dendrite-free lithium metal anode current collector, *Adv. Energy Mater.* 8 (19) (2018) 1800266.
- [27] C.J. Niu, H.L. Pan, W. Xu, J. Xiao, J.G. Zhang, L.L. Luo, C.M. Wang, D.H. Mei, J.S. Meng, X.P. Wang, Z. Liu, L.Q. Mai, J. Liu, Self-smoothing anode for achieving high-energy lithium metal batteries under realistic conditions, *Nat. Nanotechnol.* 14 (6) (2019) 594–.
- [28] D. Zhang, A. Dai, M. Wu, K. Shen, T. Xiao, G. Hou, J. Lu, Y. Tang, Lithophilic 3D porous CuZn current collector for stable lithium metal batteries, *ACS Energy Lett.* 5 (1) (2020) 180–186.
- [29] H. Liu, X. Yue, X. Xing, Q. Yan, J. Huang, V. Petrova, H. Zhou, P. Liu, A scalable 3D lithium metal anode, *Energy Storage Mater.* 16 (2019) 505–511.
- [30] X. Ke, Y. Liang, L. Ou, H. Liu, Y. Chen, W. Wu, Y. Cheng, Z. Guo, Y. Lai, P. Liu, Z. Shi, Surface engineering of commercial Ni foams for stable Li metal anodes, *Energy Storage Mater.* 23 (2019) 547–555.
- [31] X.B. Cheng, T.Z. Hou, R. Zhang, H.J. Peng, C.Z. Zhao, J.Q. Huang, Q. Zhang, Dendrite-free lithium deposition induced by uniformly distributed lithium ions for efficient lithium metal batteries, *Adv. Mater.* 28 (15) (2016) 2888–2895.
- [32] R. Weber, M. Genovese, A.J. Louli, S. Hames, C. Martin, I.G. Hill, J.R. Dahn, Long cycle life and dendrite-free lithium morphology in anode-free lithium pouch cells enabled by a dual-salt liquid electrolyte, *Nat. Energy* 4 (8) (2019) 683–689.
- [33] A. Huang, H. Liu, O. Manor, P. Liu, J. Friend, Enabling rapid charging lithium metal batteries via surface acoustic wave-driven electrolyte flow, *Adv. Mater.* 32 (14) (2020) 1907516.
- [34] C. Fang, J. Li, M. Zhang, Y. Zhang, F. Yang, J.Z. Lee, M.-H. Lee, J. Alvarado, M.A. Schroeder, Y. Yang, B. Lu, N. Williams, M. Ceja, L. Yang, M. Cai, J. Gu, K. Xu, X. Wang, Y.S. Meng, Quantifying inactive lithium in lithium metal batteries, *Nature* 572 (7770) (2019) 511–515.
- [35] J. Zheng, T. Tang, Q. Zhao, X. Liu, Y. Deng, L.A. Archer, Physical orphaning versus chemical instability: is dendritic electrodeposition of Li fatal? *ACS Energy Lett.* 4 (6) (2019) 1349–1355.
- [36] A. Kolesnikov, M. Kolek, J.F. Dohmann, F. Horsthemke, M. Börner, P. Bieker, M. Winter, M.C. Stan, Galvanic corrosion of lithium-powder-based electrodes, *Adv. Energy Mater.* 10 (15) (2020) 2000017.
- [37] K.N. Wood, E. Kazyak, A.F. Chadwick, K.-H. Chen, J.-G. Zhang, K. Thornton, N.P. Dasgupta, Dendrites and pits: untangling the complex behavior of lithium metal anodes through operando video microscopy, *ACS Cent. Sci.* 2 (11) (2016) 790–801.
- [38] D. Wang, H. Liu, M. Li, D. Xia, J. Holoubek, Z. Deng, M. Yu, J. Tian, Z. Shan, S.P. Ong, P. Liu, Z. Chen, A long-lasting dual-function electrolyte additive for stable lithium metal batteries, *Nano Energy* 75 (2020) 104889.